Optimizing Non-Rigid Registration for Scanning Transmission Electron Microscopy Image Series

Chenyu Zhang
University of Wisconsin Madison College of Engineering
Jie Feng
University of Wisconsin Madison College of Engineering
Andrew B Yankovich
University of Wisconsin Madison College of Engineering
Alexander Kvit
University of Wisconsin Madison College of Engineering
Benjamin Berkels
RWTH Aachen University
Paul Voyles (paul.voyles@wisc.edu)
University of Wisconsin Madison https://orcid.org/0000-0001-9438-4284

Research

Keywords: non-rigid registration, scanning transmission electron microscopy, image processing

Posted Date: May 23rd, 2020

DOI: https://doi.org/10.21203/rs.3.rs-27500/v1

Optimizing Non-Rigid Registration for Scanning Transmission Electron Microscopy Image Series

Chenyu Zhang[1], Jie Feng[1], Andrew B Yankovich[1], Alexander Kvit[1], Benjamin Berkels[2], Paul M Voyles[1]*

[1]Department of Materials Science and Engineering, University of Wisconsin – Madison, 1509 University Avenue, Madison, WI 53706, USA

[2]Aachen Institute for Advanced Study in Computational Engineering Science, RWTH Aachen University, Schinkelstr. 2, 52056 Aachen, Germany

*Correspondence: paul.voyles@wisc.edu

Abstract

Achieving sub-picometer precision measurements of atomic column positions in high-resolution scanning transmission electron microscope images using non-rigid registration (NRR) and averaging of image series requires careful optimization of experimental conditions and the parameters of the registration algorithm. On experimental data from $SrTiO_3$ [100], sub-pm precision requires alignment of the sample to the zone axis to within 1 mrad tilt and sample drift of less than 1 nm/min. At fixed total electron dose for the series, precision in the fast scan direction improves with shorter pixel dwell time to the limit of our microscope hardware, but the best precision along the slow scan direction occurs at 6 µs/px dwell time. Within the NRR algorithm, the "smoothness factor" that penalizes large estimated shifts is the most important

parameter for sub-pm precision, but in general the precision of NRR images is robust over a wide range of parameters.

Keywords: non-rigid registration, scanning transmission electron microscopy, image processing

1 Introduction

Scanning transmission electron microscopy (STEM) can routinely obtain images with sub-Ångstrom spatial resolution. With appropriate processing, the positions of atomic columns in these images can be measured much more precisely than the resolution, with picometer- and even sub-picometer precision reported using various approaches[1–5]. The precision here is referred to as the random variation in measurements, not the systematic difference between measurement and the truth, which is referred to as accuracy. Although the measured values could be off from the true values, we can still use the relative values to study small strains in crystalline materials one atomic column at a time has the potential to impact materials research on topics including ferroic distortions[6,7], microstructural strains[8,9], octahedral rotation angles[10,11], catalytic activities[12], and characterization of point defects[13,14].

The precision of atom positions determination is influenced by two factors: image signal-to-noise ratio (SNR)[15–17] and image distortions[2-4]. With a low-noise detector like most modern STEM detectors, SNR is determined by the electron dose, which is proportional to the exposure time at fixed beam current. Distortions in STEM refers to the fact that actual probe positions on the sample being deviated from expected perfect regular grid, and they arise from two sources: sample drift during acquisition and scan distortion. As STEM images are acquired in a pixel-by-pixel serial scan, sample drift means the sample is in different positions during the acquisition of different pixels in the frame. As a result, the final image can be sheared and sometimes uninterpretable, especially when the frame exposure time is long. Scan distortions are often

dominated by the random offset deviations at the beginning of each row in the row-wise scan pattern, which results in slicing artifacts[18], but can also result from floor vibration, acoustic noise in the microscope lab, higher-frequency instability in the scan electronics, and variation of focus and sample z-height from STEM instabilities.

Both high electron dose and minimum scan distortions are necessary to obtain a high precision image. A common way to achieve both is to acquire a series of fast acquisition frames in which every single frame has small distortion, register the frames to one another to computationally compensate for sample drift, then average the registered frames to get a single high-quality image. Kimoto *et al.* reported several pm precision with simple drift detection and compensation using cross-correlation and rigid shifts that move all the pixels in a single frame by the same vector[19]. Berkels *et al.* used non-rigid registration (NRR) to align STEM images.[20] In NRR, every pixel in each frame has its own shift vector, which better fits the serial, pixel-by-pixel acquisition scheme of STEM. Yankovich *et al.* reported sub-pm precision images from high angle annular dark-field (HAADF) image series after post-acquisition alignment using NRR[1]. Jones and Nellist developed an NRR algorithm combining registration with prior knowledge of atomic features to remove scan distortions[4]. Berkels and Liebscher improved NRR to remove the bias toward the keyframe in the image series[21]. Ning et al[22], Sang and LeBeau[2], and Ophus and Ciston[3] use a series of images of the same sample area acquired with different scan directions to provide additional information for NRR correction of scan distortions, leading to sub-pm precision. Compared to these methods, NRR has the advantage of not customized acquisition software or hardware, but it is more sensitive to systematic errors like a non-square scan grid.

Here, we focus on optimizing experimental parameters and the Berkels NRR algorithm on the HAADF STEM image series to obtain a sub-pm precision final image. The algorithm is described in detail elsewhere[20]. Experiment requirements for high-quality input image series are described in Section 2.1, with the NRR algorithm and the definition of precision introduced in Section 2.2. Examples of NRR results are shown in Section 3.1. Registration parameters are tested and discussed in Section 3.2, and Section 3.3 focuses on directly visualizing the registration between frames and possible artifacts from problematic parameter selections. In the end, Section 3.4 discusses how to use NRR under a given fixed electron dose effectively.

2 Methods

2.1 Experiment

A $SrTiO_3$ [100] single crystal sample was prepared by wedge polishing at a 1.6° angle using an Allied MultiPrep Polishing system with diamond lapping films, using lapping film particle sizes decreasing from 15 μm to 0.1 μm step by step. The sample was then ion milled from both sides at 5° angle in a Fischione model 1050 TEM mill using an Ar ion beam. A 3kV ion beam was used at the beginning step, followed by successively decreased voltages ending at 100V. The sample was kept under vacuum and plasma cleaned before being inserted into the TEM column. The column and the inserted sample were cleaned with an on-column GV10x Gentle Asher plasma cleaner to reduce contamination during the long acquisition of the image series.

A Thermo-Fisher Titan STEM equipped with a CEOS probe aberration corrector operated at 200 kV was used to collect image series for NRR. STEM image series were collected with a 24.5 mrad probe semi-angle and 18.9 pA probe current. 256 by 256 pixel HAADF STEM image series were acquired on a Fischione Model 3000 detector spanning 53.9 and 270 mrad. 8 μs pixel

dwell time (1.99×10^4 $e^-/Å^2$ frame dose) was used as a standard dwell time for experiments on sample tilt and optimization of NRR parameters. 0.5 µs to 12 µs (1.24×10^3 $e^-/Å^2$ to 2.99×10^4 $e^-/Å^2$ dose/frame) pixel dwell times were used to study the precision as a function of dwell time, with a variable number of frames to maintain constant dose. Line synchronization of the scan was not used during acquisition, as we want the distortion to be different in each image and thus average out of the series, rather than being the same because it is synchronized to the line frequency.

Considering the long total exposure time, the sample was stabilized for more than three hours to minimize sample drift before image series acquisition. Drift better than 1 nm/min was routinely achieved, and drift better than 1 Å/min was achievable for an extremely stable sample if stabilizing long enough. A small sample drift is important to get a large field of view in the final registered image, as only the area that is inside the viewing window throughout the image series will be used in the final registered image. Thin and uniform are with about 20 nm thickness was used to acquire HAADF image series. The fast scan direction (horizontal rows in the images) is aligned with the $SrTiO_3$ [010] of $SrTiO_3$ lattice, and standard deviations of Sr column spacings along [010] and [001] direction are defined as image precisions on the fast scan and the slow scan direction. Residual aberrations were corrected manually to get round shaped atomic columns with no elongations and a good contrast between atomic columns and the background on the atomic resolution image.

2.2 NRR and precision analysis

The NRR algorithm registers a target frame to the keyframe by finding an optimal set of deformations ϕ_{NR}, which consists of a separate vector for each pixel in the target frame. The

deformation is supposed to capture the sample drift between the acquisition of the target frame and the keyframe. The deformation is determined by optimizing an energy function

$$E[\phi_{NR}] = E_{NCC}[\phi_{NR}] + \frac{\lambda}{2}\int_{\Omega} \|D\phi_{NR}(x) - \mathbf{1}\|^2 dx, \qquad [1]$$

which contains the negative normalized cross-correlation between the registered/deformed target frame and the keyframe (first term) and the Dirichlet energy of the deformation (second term). The first term quantifies the difference between the keyframe and the registered target frame, and the second is a regularizer that penalizes abrupt changes in the deformation. The image domain Ω is normalized to have the area of a unit square so that the number of pixels on the image won't change the value of the energy function. A smoothness factor λ is used to balance the weights of the two terms. The energy function is minimized using a multilevel, regularized gradient descent method to find the optimal deformation[20]. "Multilevel" means that the images are first downsampled, for example, from 256×256 pixels to 64×64 pixels. The downsampled versions are registered, and the deformations from low pixel count registration are used as initial guesses for the registration at the next finer level, iterating back up to the original number of pixels. Deformations of large structures covering more pixels, caused by example by sample drift, are captured at low pixel count, while deformations of small structures affecting fewer pixels, caused for example by acoustic noise, are captured at high pixel count.

After the whole image series is registered, registered frames are averaged to produce one single high-quality frame with frame dose equal to the total dose of the image series. This frame is then cropped to retain only the region that remains in the STEM field of view throughout the acquisition, making it smaller than a single raw frame and often rectangular. Sr atom sites in the final image are used for precision analysis. The atomic column positions are determined by

performing least-square fittings around each Sr site, which fits each Sr peak to an asymmetric 2D Gaussian function with a constant background[1].

Precision in this study is defined as the standard deviation of a repeated, known crystallographic distance in the image[23]. Strain measurement has also been used as a metric for precision, in which case a small measured strain in a nominally strain-free crystal means high precision[18]. Both metrics assume that the lattice is perfectly periodic, and any aperiodic structure is a result of an imperfect image. Both metrics can only be applied to perfect single crystal samples without impurities or strain introduced by sample preparation.

3 Results and discussion

3.1 Registration results

Figure 1(a)-(c) shows the results from an on-zone high-quality image series acquired on $SrTiO_3$ [100] single crystal sample. Figure 1(a) is an example of a single frame in the image series, which has limited SNR and some clear slicing artifacts from scan distortions. Figure 1(b) is the final image after NRR with improved SNR and no visual sign of residual scan distortion. It has 0.57 pm precision along the fast scan direction and 0.77 pm precision along the slow scan direction. The somewhat poorer precision along the slow scan direction could be from a long time between pixels (the line acquisition time, rather than the pixel dwell time), but this is inconsistent with the results in Section 3.4 below. Instead, we believe it may arise from residual flyback error not corrected by the registration, or the fact that the drift was primarily in the y direction. Figure 1(c) shows the position averaged convergent beam electron diffraction (PACBED) pattern acquired from the same region together with the image series, which is very

close to the [100] zone axis and shows a highly symmetric pattern. By estimating the distance between the center of Bragg diffractions and the center bright disk, we estimate the tilt from [100] zone axis to be less than 1 mrad.

Figure 1 (d)-(f) show a single frame, the final image, and the PACBED pattern acquired with the sample tilted by ~6.3 mrad from [100] zone axis, estimated by eye from the PACBED pattern. At this tilt, the atomic columns in Figure 1(d) and (e) show clear elongation along one direction and reduced contrast between the bright atomic columns and the dark background. Figure 1(e) has 1.67 pm precision along the fast scan direction and 1.79 pm precision along the slow scan direction. It is difficult to control the tilt precisely to perform a systematic experiment as a function of tilt along a particular direction, but experience across many experiments at different random tilts suggests that sub-pm precision is only obtained for off-zone tilts of 1 mrad or less.

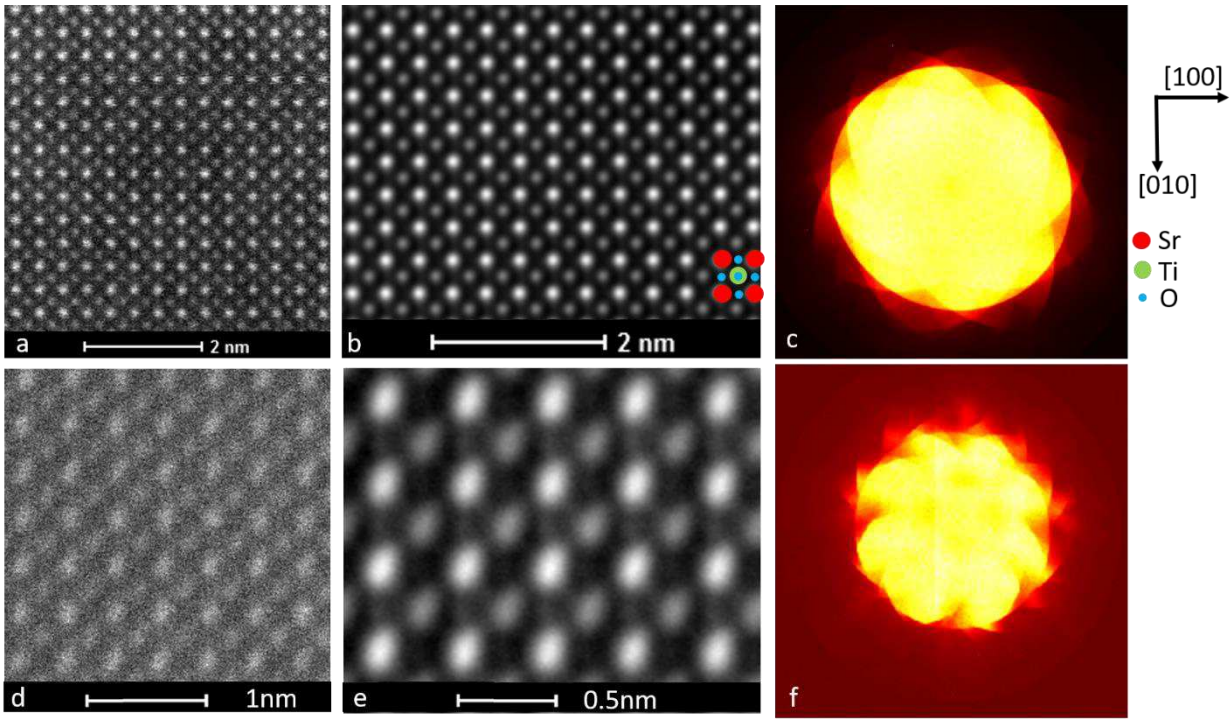

Figure 1 (a) single HAADF acquisition, (b) averaged image after registration and cropped according to sample drift, (c) PACBED pattern with the center bright disk corresponding to 24.5 mrad convergence

angle from an on zone axis $SrTiO_3$ sample. (d-f) shows the single frame, final image, and PACBED pattern for a tilted sample

3.2 Registration parameters

The NRR algorithm has five tunable parameters: the smoothness factor λ shown in eq [1], and parameters controlling the multilevel registration scheme, the number of registration iterations, and the convergence criterion. A detailed description of these parameters can be found in ref 20[20]. Table 2 lists all the parameters with a brief definition, the allowed range of values, and a recommended value for each one derived from parameter optimizations by varying one parameter at a time with other parameters fixed. Each parameter's effect on the precision of the final image after NRR on the 8 μs dwell time $SrTiO_3$ data was tested by varying one parameter at a time with the other parameters fixed at the recommended value.

Table 2. List of all parameters in NRR with their definitions, possible ranges, and recommended values.

Name	Definition (assume single raw frame has 2^n by 2^n pixels)	Range	Recommend value
Smoothness factor (λ in eq [1])	Controls the relative importance of the smoothness term in the energy, eq [1]	>0	200
Start level	Images for the first level of registration will be downsampled to $2^{\text{start level}} \times 2^{\text{start level}}$ pixels	An integer between 1 and n for input images of $2^n \times 2^n$ pixels.	n-1

λ multiplier	Multiplier to λ for registration of data on a grid downsampled by a factor of 2	>0	5
Convergence criterion	Stopping threshold for energy minimization	>0	10^{-6}
Total iterations	The number of total NRR iterations including the initial stage and following refining stages.	integer ≥ 1	3

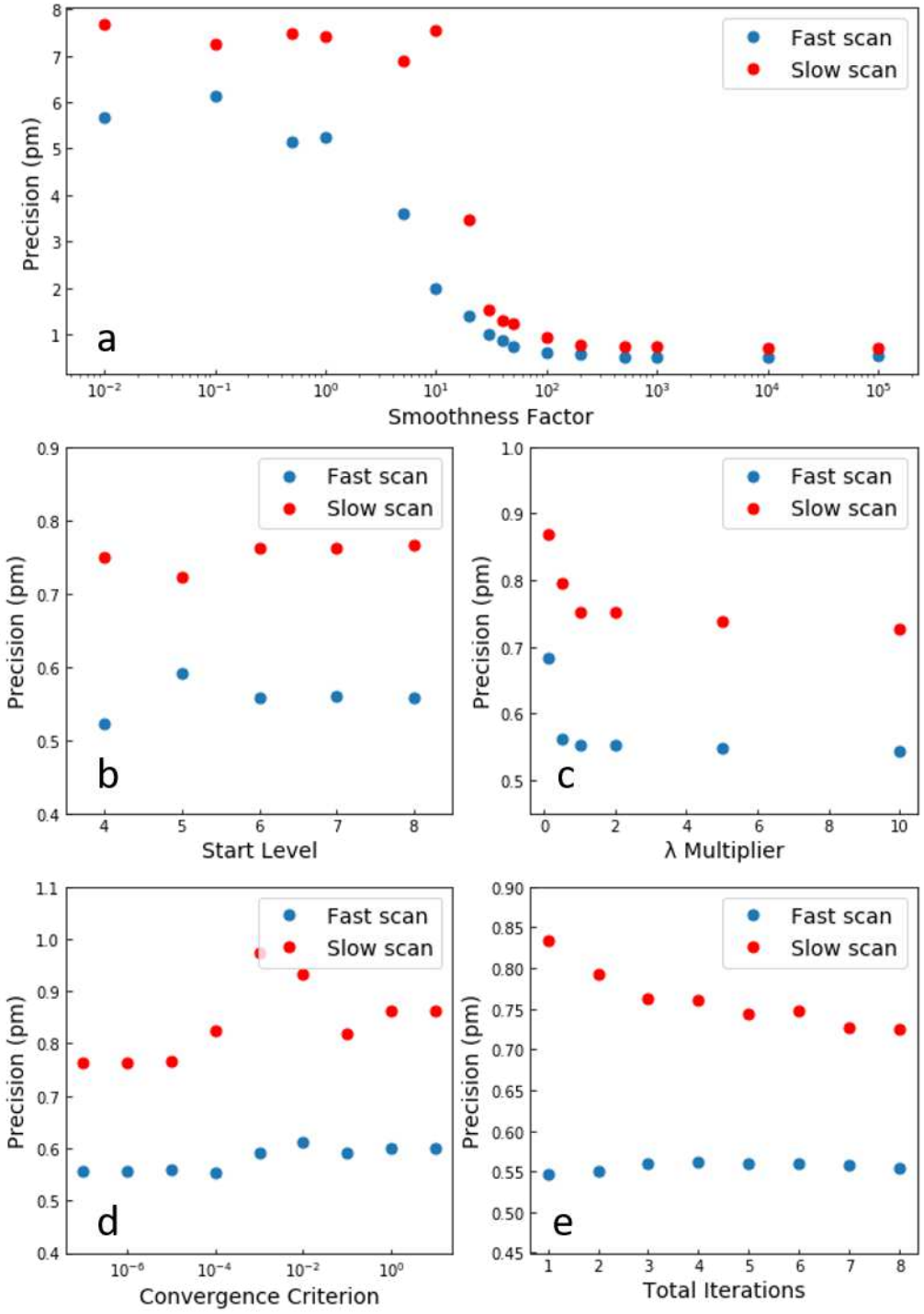

Figure 2 Effect of (a) λ, (b) registration start level, (c) λ multiplier, (d) convergence criterion, and (e) total iterations on the precision of the final image.

Figure 2 shows the effect of all five parameters on the precision of the final registered image. Smoothness factor has the most noticeable effect on the final precision, as shown in Figure 2(a). Result suggests that a λ above 100 is enough to achieve sub-pm precision. A smaller λ causes worse precision and, as shown in Section 3.3, obvious artifacts in the deformations. Precision does not improve significantly with λ>200. The fairly large optimal λ suggests that the dominant drift pattern in the images is smooth over a significant number of pixels. We recommend a default λ of 200.

Figure 2(b) shows precision from different registration start levels. Start level controls the downsampling in the multilevel registration, which is used to avoid unwanted local minimum (described in detail in ref 19[20]). The NRR algorithm takes square images with side lengths in pixels a power of two (2^n along each side), and the downsampling procedure is processed by a factor of 2 at each step. With given start level k, the side length in number of pixels used at the beginning of the registration is

$$n_{downsampled} = \frac{n_{original}}{2^{n-k}}, \quad [2]$$

where $n_{original}$ is the side length in the raw image series. Sub-pm precisions are achieved under all different start levels. When using a small start level, the image at the beginning of the registration may lose all the features that could be used for registration, especially for atomic resolution images on the periodic lattice structure. In this case, a possible registration artifact is a large jump by half or a full repeating unit. An example of this artifact will be discussed in Section 3.3. We recommend a default start level of n-1, however, if the pixel size is much smaller than what we are using (21.5 pm/px), a smaller start level might be beneficial or even necessary.

Figure 2(c) shows the effect of the λ multiplier. Downsampled registrations are performed with a smoothness factor of (λ multiplier)^r×λ, where $r = \log_2(\frac{n}{n_{downsampled}})$ is the number of times the original data have been downsampled by a factor of 2. λ multiplier larger than 1 means smoothness of deformation is emphasized more when registering with a coarser pixel grid. Result suggests that a λ multiplier larger than 1 is preferred, but that the final precision improves only slowly with λ multipliers larger than 1. We recommend a default λ-factor of 5.

Figure 2 (d) and (e) show the effects of the convergence criterion and the total iterations. The convergence criterion controls when to stop the optimization of energy function [1]. The number of total iterations controls the number of times the algorithm registers the image series, including the initial stage, and re-registration stages using the output of the previous registration as the initial guess for the current registration. Results suggest that a convergence criterion of 10^{-6} with a total of 3 iterations is enough for sub-pm precision.

3.3 Visualization of Artifacts

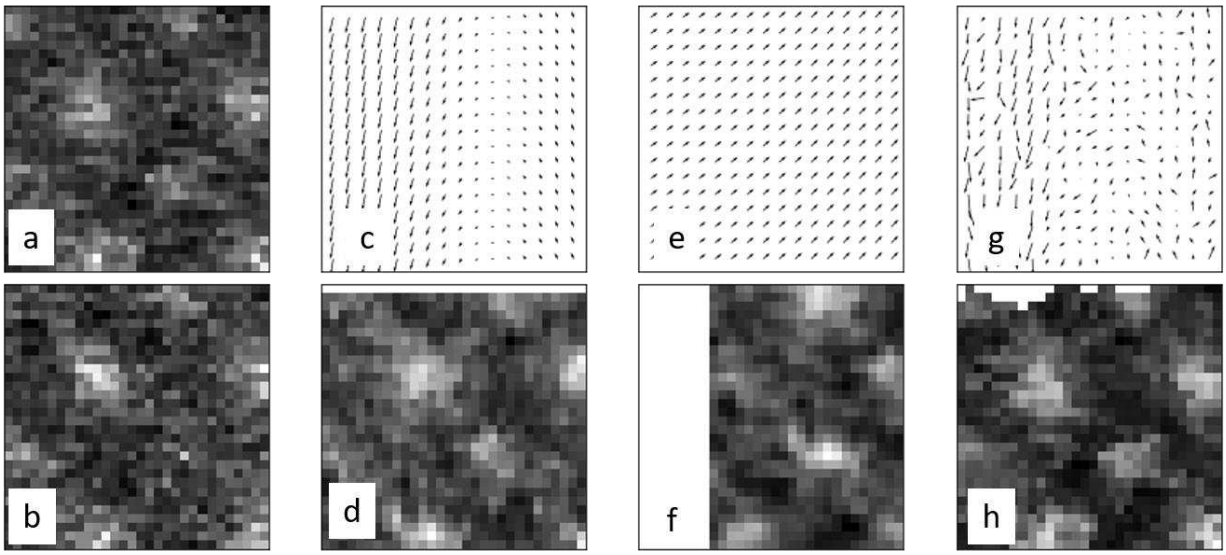

Figure 3 Example of the deformation field for registration between two frames under various conditions. (a) and (b) are small patches of the original frames. (a) is the keyframe, and (b) will be deformed to match it. (c) and (d), (e) and (f), and (g) and (h) are pairs of deformation vector fields (c, e, and g) and deformed images (d, f, and h) processed with various choices of registration parameters. (c) and (d) use the default parameter, (e) and (f) used a too small start level, and (g) and (h) used a too small lambda value.

Figure 3 shows examples of non-rigid pixel deformations determined by NRR using different parameter settings. In each case, NRR seeks the deformation to register the target frame shown in figure 3(b) to the keyframe shown in figure 3(a). Figures 3(c), (e), and (g) show the vector plots of non-rigid pixel deformations determined under the default parameter, a (too) small start level, and a (too) small lambda value, respectively. All three plots are shown at reduced pixel density (344 pm spacing between vectors) for the whole frame. Figures 3(d), (f), and (h) show the deformed frames after applying the deformation.

Figure 3(c) and (d) show the deformation under optimal conditions. The vector field is smooth, primarily capturing the effects of sample drift, with small contributions from higher-frequency distortions that are not really visible in the figure. On a stable sample in thermal equilibrium with our microscope, the sample drift is a random walk with no consistent direction, which leads to the smoothly varying but not constant deformation field in figure 3(c). Figure 3(d) shows the registered image patch where the whole registered image patch moves a few pixels to match the keyframe shown in figure 3(a), but it does not simply duplicate all the features in the keyframe such as the slicing artifacts from scan distortions.

Figure 3(e) and (f) show the deformation and registered image patch when the image was downsampled too much at the beginning step. The image with 256 px side length was downsampled to 8 px at the beginning of registration, resulting in an image series with 688 pm pixel size at the beginning stage of registration, larger than the lattice parameter of $SrTiO_3$ (390.5 pm). In this case, each pixel in the image was larger than a single unit cell, and the whole downsampled image had little to no features to be registered. As a result, the NRR algorithm made a half unit-cell jump that registered the Sr atom sites in the target frame to Ti sites in the keyframe. Note that this artifact does not occor for a reasonable choice of start level that is sufficiently large like the one we recommended in Section 3.2, and also could be avoided if the image had a large scale feature such as an interface, surface, or grain boundary, which provides registration references at large pixel sizes.

Figure 3(g) and (h) show the deformation from a small λ value, in which NRR determined an unsmooth deformation. The registered image patch in figure 3(h) looks very similar to the keyframe, but it preserves all the scan distortions, as atomic columns in the registered image have exactly the same slicing artifact as the keyframe. This represents overfitting, since we want

to average out rather than preserve high-frequency distortions. We also suspect that some pixels could be shifted to match pixels that are bright in the keyframe due to random noise, not variations in sample scattering. Preserving scan distortion and noise reduces the precision in the averaged image.

3.4 Selection of pixel dwell time / frame dose

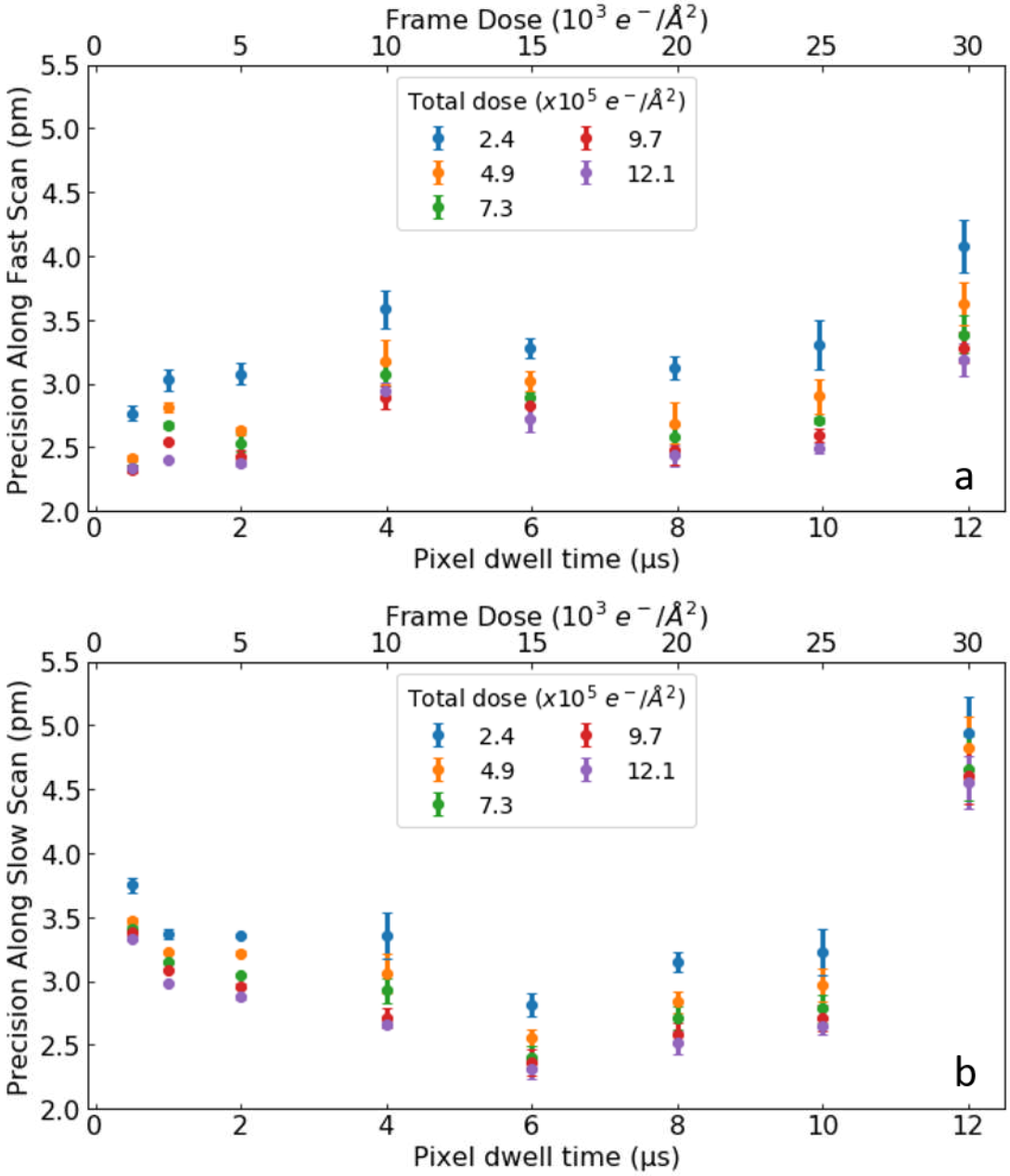

Figure 4 Registered averaged image precision along (a) fast scan and (b) slow scan direction under different pixel dwell time / frame dose. The total dose is kept constant by varying the number of registered images.

High precision STEM via series acquisition and NRR is inherently a high-dose method, but the total electron dose a given sample can sustain is often limited. (*e.g.* [24] and [25]). There are two different ways to split a given dose into multiple frames at fixed pixel sampling: 1. Use a longer pixel dwell time and fewer frames. In this case, each frame has a higher SNR and clear features for registration, but each pixel can average over faster distortions that cannot be corrected by NRR, and the series contains a small number of samples of distortions. 2. Use a shorter dwell time and more frames. In this case, each frame has lower SNR and less clear features, but each one provides better sampling of the distortions at different time scales, and the series contains a larger number of distortion samples. Dose can also be varied by using large pixels to reduce the dose or smaller pixels to increase the dose. High signal to noise images at much lower dose than used here can still be achieved with very large pixels, but the precision suffers is ~4 pm, rather than <1 pm.[27] The effect of pixel size has not been studied systematically here.

Different ways to use a fixed total electron dose budget have been studied on $SrTiO_3$ [100] image series acquired with frame doses ranging from 1.2×10^3 $e^-/Å^2$ to 2.5×10^4 $e^-/Å^2$, varied by using pixel dwell times from 0.5 µs to 12 µs at fixed beam current. Pixel dwell times shorter than 0.5 µs/px were not tested as they cause large, systematic scan distortion on our microscope[26]. Five different total electron doses ranging from 2×10^5 $e^-/Å^2$ to 12×10^5 $e^-/Å^2$ were studied by varying the total numbers of frames used. All the image series were registered with recommended parameters described in Table 2.

Figure 4 shows precision along the fast scan direction and the slow scan direction vs. pixel dwell time for the five different total doses. All these data were acquired with a relatively low electron dose compare to the results shown in Section 3.1 and 3.2, which is why we do not have sub-pm precision on all these image series. Both scan directions show improved precisions with a higher

total dose under all different frame doses. Under a fixed total electron dose, a short pixel dwell time of 0.5 µs/px (1.25×10^3 $e^-/Å^2$ frame dose) is best for the fast scan direction precision. Even shorter dwell time might be better, but cannot be tested on our microscope. We suspect that faster scanning means improved precision because faster scanning means that the images capture, rather than averaging over, a broader frequency range of distortions. A longer pixel dwell time of 6 µs/px (1.5×10^4 $e^-/Å^2$ frame dose) is best for the slow scan direction precision. We speculate that this effect arises because of some imperfection in the scan that grows worse at short pixel dwell time, like a random vertical offset of the pixel created by imprecise flyback at the end of the line. The fast scan direction has a local minimum in the precision at 8 µs, which might arise from the same source. At longer than 10 µs/px, precision along both scan directions grows worse. We speculate that this is a result of longer acquisition times averaging over fast distortions within each frame, making them uncorrectable by NRR. On balance, we recommend 6 or 8 µs pixel dwell time as optimal for high precision imaging using NRR. However, if the optimal pixel dwell time is influenced by microscope non-idealities and instability as we guess, it will vary from instrument to instrument and lab to lab.

4 Conclusion

Experimental requirements and NRR algorithm parameters to achieve sub-pm precision have been studied using atomic resolution HAADF image series acquired on a $SrTiO_3$ [100] single crystal sample. Sub-pm precision requires less than 1 mrad off-zone tilt and less than 1 nm/min sample drift. The smoothness factor parameter is the most important to precision after NRR, and a sufficiently large value (larger than 100 in this study) is shown to be the key factor for high precision. We derive the recommended default values for all the parameters as a result of our

parameter study. Large deviations from these parameters can create artifacts in the registration, while in general NRR precisions are robust over a wide range of parameter selections. When applying NRR to image series with fixed total electron dose, the precision is best along the fast scan direction at the shortest accessible pixel dwell time, but the precision along slow scan direction is best at a pixel dwell time of 6 µs/px. On balance, 6 to 8 µs / pixel is the optimal pixel dwell time. With these conditions and careful acquisition, sub-picometer precision on samples that can sustain a high electron dose is routinely achieved.

5 List of Abbreviations

NRR: non-rigid registration

STEM: scanning transmission electron microscopy

SNR: signal-to-noise ratio

HAADF: high angle annular dark-field

PACBED: position averaged convergent beam electron diffraction

6 Declarations

Availability of data and materials

All the raw data, registration parameter files, registration results, and code for data analysis are available via the Materials Data Facility https://doi.org/10.18126/1h93-n56i. Code for data analysis are also available on Github (https://doi.org/10.5281/zenodo.3723363). The non-rigid registration software can be accessed on the Nanohub online app: https://nanohub.org/tools/nrr. NRR source code is owned by Benjamin Berkels and is released on https://github.com/berkels/match-series.

Competing interests

The author declares that they have no competing interests.

Funding

This work was support by the US Department of Energy, Basic Energy Sciences (DE-FG02-08ER46547) and used facilities supported by the Wisconsin MRSEC (DMR-1720415).

Authors' contributions

C.Z, J.F, A.B.Y, and A.K acquired the STEM experiment data, C.Z performed NRR and data analysis, B.B supported the registration code, P.M.V supervised the work.

Acknowledgements

Not applicable.

1. Yankovich, A. B. *et al.* Picometre-precision analysis of scanning transmission electron microscopy images of platinum nanocatalysts. *Nat. Commun.* **5**, 4155 (2014).

2. Sang, X. & LeBeau, J. M. Revolving scanning transmission electron microscopy: Correcting sample drift distortion without prior knowledge. *Ultramicroscopy* **138**, 28–35 (2014).

3. Ophus, C., Ciston, J. & Nelson, C. T. Correcting nonlinear drift distortion of scanning probe and scanning transmission electron microscopies from image pairs with orthogonal scan directions. *Ultramicroscopy* **162**, 1–9 (2016).

4. Jones, L. & Nellist, P. D. Identifying and correcting scan noise and drift in the scanning transmission electron microscope. *Microsc. Microanal.* **19**, 1050–60 (2013).

5. Jones, L. *et al.* Smart Align—a new tool for robust non-rigid registration of scanning microscope data. *Adv. Struct. Chem. Imaging* **1**, 8 (2015).

6. Rojac, T. *et al.* Domain-wall conduction in ferroelectric BiFeO3 controlled by accumulation of charged defects. *Nat. Mater.* **16**, 322–327 (2016).

7. Lee, D. *et al.* Emergence of room-temperature ferroelectricity at reduced dimensions. *Science (80-.).* **349**, 1314–1317 (2015).

8. Tang, Y. L., Zhu, Y. L. & Ma, X. L. On the benefit of aberration-corrected HAADF-STEM for strain determination and its application to tailoring ferroelectric domain patterns. *Ultramicroscopy* **160**, 57–63 (2015).

9. Oni, A. A. *et al.* Large area strain analysis using scanning transmission electron microscopy across multiple images. *Appl. Phys. Lett.* **106**, (2015).

10. Borisevich, A. Y. *et al.* Mapping octahedral tilts and polarization across a domain wall in BiFeO3 from Z-contrast scanning transmission electron microscopy image atomic column shape analysis. *ACS Nano* **4**, 6071–6079 (2010).

11. Wang, Y., Salzberger, U., Sigle, W., Eren Suyolcu, Y. & van Aken, P. A. Oxygen octahedra picker: A software tool to extract quantitative information from STEM images. *Ultramicroscopy* **168**, 46–52 (2016).

12. Nilsson Pingel, T., Jørgensen, M., Yankovich, A. B., Grönbeck, H. & Olsson, E. Influence of atomic site-specific strain on catalytic activity of supported nanoparticles. *Nat. Commun.* **9**, (2018).

13. Hwang, J., Zhang, J. Y., D'Alfonso, A. J., Allen, L. J. & Stemmer, S. Three-Dimensional Imaging of Individual Dopant Atoms in <math display="inline"> <msub> <mi>SrTiO</mi> <mn>3</mn> </msub> </math>. *Phys. Rev. Lett.* **111**, 266101 (2013).

14. Feng, J., Kvit, A. V., Zhang, C., Morgan, D. & Voyles, P. M. Three-Dimensional Imaging of Single La Vacancies in LaMnO 3. *Microsc. Microanal.* **22**, 902–903 (2016).

15. Van Aert, S., den Dekker, a J., Van Dyck, D. & van den Bos, a. Optimal experimental design of STEM measurement of atom column positions. *Ultramicroscopy* **90**, 273–89 (2002).

16. De Backer, a., Martinez, G. T., Rosenauer, A. & Van Aert, S. Atom counting in HAADF STEM using a statistical model-based approach: Methodology, possibilities, and inherent limitations. *Ultramicroscopy* (2013). doi:10.1016/j.ultramic.2013.05.003

17. De Backer, A. *et al.* Dose limited reliability of quantitative annular dark field scanning

transmission electron microscopy for nano-particle atom-counting. *Ultramicroscopy* 1–6 (2014). doi:10.1016/j.ultramic.2014.11.028

18. Jones, L. *et al.* Optimising multi-frame ADF-STEM for high-precision atomic-resolution strain mapping. *Ultramicroscopy* **179**, 57–62 (2017).

19. Kimoto, K. *et al.* Local crystal structure analysis with several picometer precision using scanning transmission electron microscopy. *Ultramicroscopy* **110**, 778–782 (2010).

20. Berkels, B. *et al.* Optimized imaging using non-rigid registration. *Ultramicroscopy* **138**, 46–56 (2013).

21. Berkels, B. & Liebscher, C. H. Joint non-rigid image registration and reconstruction for quantitative atomic resolution scanning transmission electron microscopy. *Ultramicroscopy* **198**, 49–57 (2019).

22. Ning, S. *et al.* Scanning distortion correction in STEM images. *Ultramicroscopy* **184**, 274–283 (2017).

23. Bals, S., Van Aert, S., Van Tendeloo, G. & Ávila-Brande, D. Statistical estimation of atomic positions from exit wave reconstruction with a precision in the picometer range. *Phys. Rev. Lett.* **96**, 096106 (2006).

24. Zhang, D. *et al.* Atomic-resolution transmission electron microscopy of electron beam–sensitive crystalline materials. *Science (80-.).* **359**, 675–679 (2018).

25. Kotakoski, J., Jin, C. H., Lehtinen, O., Suenaga, K. & Krasheninnikov, A. V. Electron knock-on damage in hexagonal boron nitride monolayers. *Phys. Rev. B* **82**, 113404 (2010).

26. Buban, J. P., Ramasse, Q., Gipson, B., Browning, N. D. & Stahlberg, H. High-resolution low-dose scanning transmission electron microscopy. *J. Electron Microsc. (Tokyo).* **59**, 103–112 (2010).

27. Yankovich, A. B., Berkels, B., Dahmen, W., Binev, P. & Voyles, P. M. High-precision scanning transmission electron microscopy at coarse pixel sampling for reduced electron dose. *Adv. Struct. Chem. Imaging* **1**, 2 (2015).

Figures

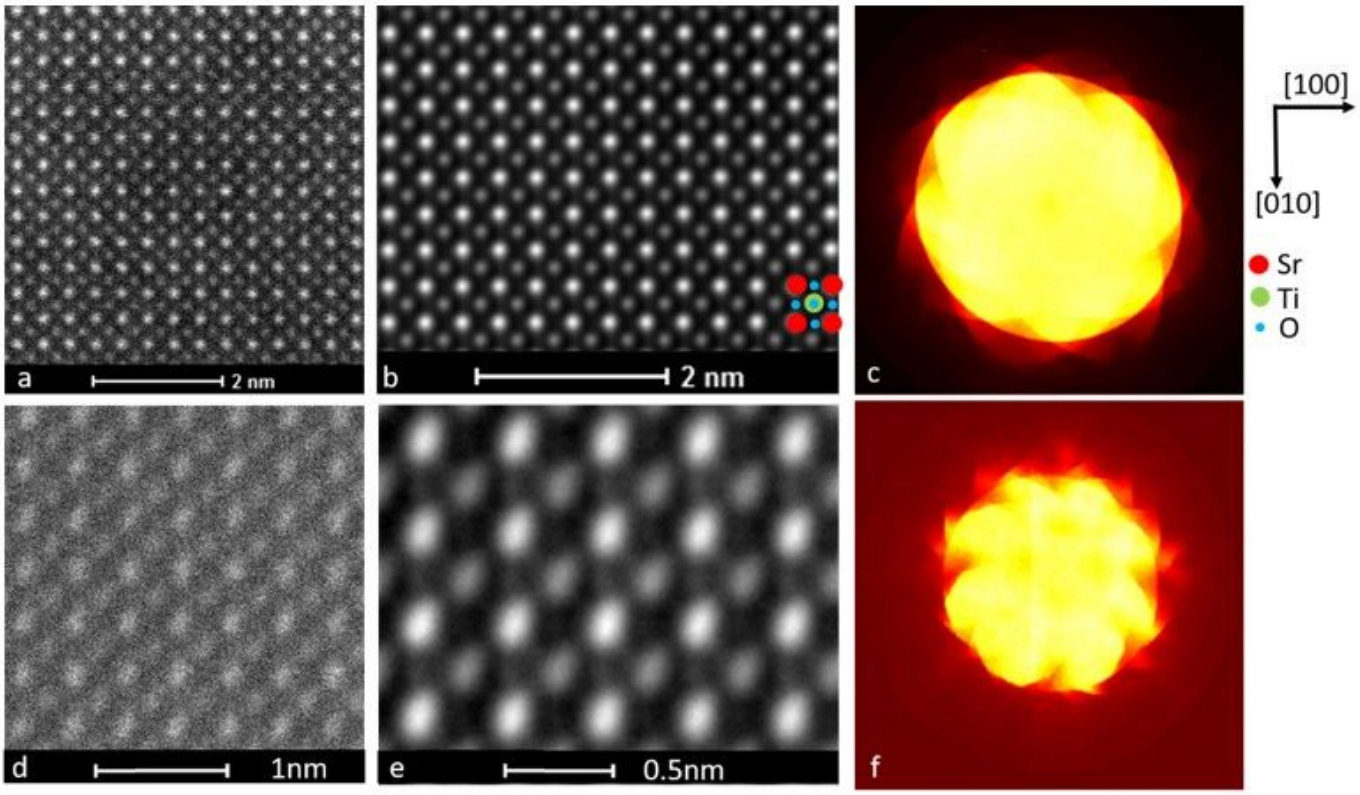

Figure 1

(a) single HAADF acquisition, (b) averaged image after registration and cropped according to sample drift, (c) PACBED pattern with the center bright disk corresponding to 24.5 mrad convergence angle from an on zone axis SrTiO3 sample. (d-f) shows the single frame, final image, and PACBED pattern for a tilted sample

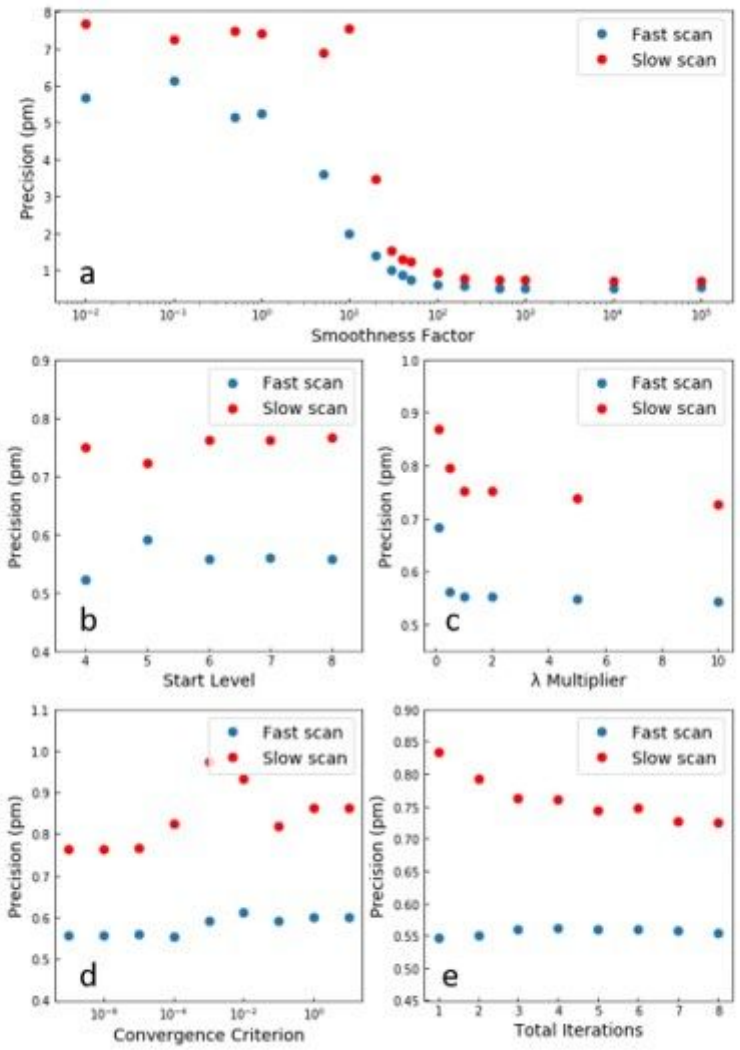

Figure 2

Effect of (a) λ, (b) registration start level, (c) λ multiplier, (d) convergence criterion, and (e) total iterations on the precision of the final image.

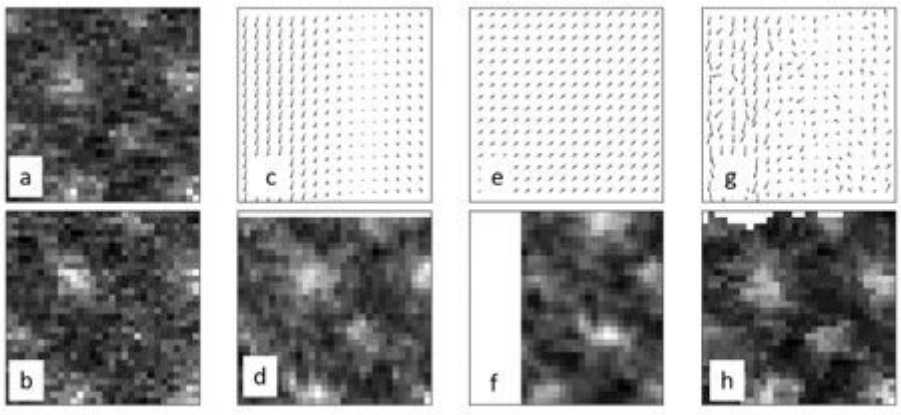

Figure 3

Example of the deformation field for registration between two frames under various conditions. (a) and (b) are small patches of the original frames. (a) is the keyframe, and (b) will be deformed to match it. (c) and (d), (e) and (f), and (g) and (h) are pairs of deformation vector fields (c, e, and g) and deformed images (d, f, and h) processed with various choices of registration parameters. (c) and (d) use the default parameter, (e) and (f) used a too small start level, and (g) and (h) used a too small lambda value.

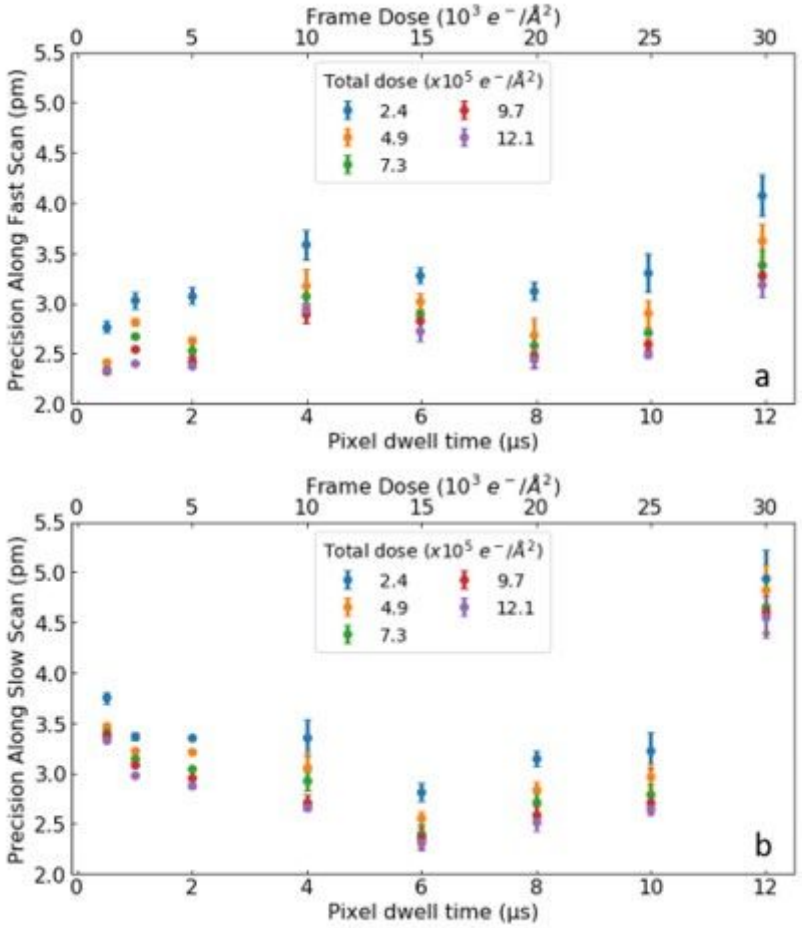

Figure 4

Registered averaged image precision along (a) fast scan and (b) slow scan direction under different pixel dwell time / frame dose. The total dose is kept constant by varying the number of registered images.